Thermal-error regime in high-accuracy gigahertz single-electron pumping

R. Zhao,[1,*] A. Rossi,[2] S. P. Giblin,[3] J. D. Fletcher,[3] F. E. Hudson,[1] M. Möttönen,[4] M. Kataoka,[3] and A. S. Dzurak[1]

[1] *School of Electrical Engineering and Telecommunications, University of New South Wales, Sydney, New South Wales 2052, Australia*

[2] *Cavendish Laboratory, University of Cambridge, J J Thomson Avenue, Cambridge CB3 0HE, United Kingdom*

[3] *National Physical Laboratory, Hampton Road, Teddington, Middlesex TW11 0LW, United Kingdom*

[4] *QCD Labs, COMP Centre of Excellence, Department of Applied Physics, Aalto University, 00076 AALTO, Finland*

(Dated: March 16, 2017)

Single-electron pumps based on semiconductor quantum dots are promising candidates for the emerging quantum standard of electrical current. They can transfer discrete charges with part-per-million (ppm) precision in nanosecond time scales. Here, we employ a metal-oxide-semiconductor silicon quantum dot to experimentally demonstrate high-accuracy gigahertz single-electron pumping in the regime where the thermal excitation of electrons, during the equilibrium charge capturing process, is the predominant error mechanism. Despite severe drive-induced heating in one of the electron reservoirs, the large addition energy of the quantum dot efficiently suppresses the thermal errors to an extremely low level. In a measurement with traceability to primary voltage and resistance standards, the averaged pump current over the quantized plateau, driven by a 1 GHz sinusoidal wave in the absence of magnetic field, is equal to the ideal value of ef within a measurement uncertainty as low as 0.27 ppm.

arXiv:1703.04795v1 [cond-mat.mes-hall] 14 Mar 2017

I. INTRODUCTION

Single-electron (SE) pumps can generate quantized electrical current by syncing the transport of individual electrons to an external periodic drive [1, 2]. These devices relate the pumped direct current, I, to the elementary charge, e, and the driving signal frequency, f, through the expression, $I = nef$, where n is an integer. As an on-demand SE source, they can be useful in the context of quantum information processing as well as in the study of fermionic optics [3–5]. Arguably, the most important application of this technology is to realize a quantum standard of electrical current [6].

Single-electron pumps and turnstiles have been realized in various physical systems, including normal-metal tunnel junction devices [7, 8], surface accoustic wave devices [9, 10], superconducting devices [11–13], hybrid superconductor-normal-metal turnstiles [14], quantum dots [15–27] and single dopants [28–31]. The tunable-barrier SE pumps based on semiconductor quantum dots (QDs) stand out from the competing technologies for providing a good balance between low pumping error and high output current [17, 25, 27, 32, 33]. Three different designs of GaAs pumps have achieved relative errors close to or below 1 part per million (ppm) in high-accuracy measurements traceable to primary standards [17, 18, 32, 33]. These GaAs pumps transport a fixed number of electrons per cycle following a series of sequential back-tunneling events, known as the decay cascade [34]. Previous studies indicate that strong magnetic fields, tailored waveform drives and subkelvin temperatures are required for the GaAs pumps to achieve ppm level accuracy at gigahertz pumping frequencies [17, 32, 33]. These requirements render the realization of the quantum current standard demanding and restrict the user base of SE pump technology.

In contrast, QD pumps in silicon alleviate some of these burdens. Compared to depletion mode GaAs QDs, the gate voltage-induced silicon QDs tend to have a larger addition energy due to their smaller physical size. This feature of the compact silicon devices enables high frequency accurate SE pumping without arbitrary waveform drives or high magnetic fields [25, 27]. The remarkable results recently achieved in silicon devices not only demonstrate the universality of SE pumping in the tunable-barrier QDs at sub-ppm uncertainty, but also clearly indicate that a compact silicon SE pump may pave the way towards a more practical quantum standard of electrical current [27]. From a pragmatic point of view, it is advantageous to implement the quantum current standard in silicon, since it is compatible with the metal-oxide-semiconductor (MOS) technology widely employed in industry. Through well-established fabrication techniques, silicon SE pumps can be seamlessly integrated with peripheral control circuits to deliver a cost-effective on-chip current standard.

One challenge for the SE pumps is that the large rf drive amplitude usually required at gigahertz pumping frequency, may heat the electron reservoir up to temperatures of the order several Kelvins, and result in excessive thermal errors [24, 35]. When the electron reservoir temperature increases, forward tunneling of thermally excited electrons from the reservoir into the QD becomes significant during the charge capturing process, and the number of electrons trapped in the QD reflects the Fermi distribution of electrons in the leads [36]. To achieve a robust high-speed silicon-based quantum current standard, operating accurately even with electron reservoir tem-

* ruichen.zhao@student.unsw.edu.au

peratures of few Kelvins, it is important to demonstrate an effective method to suppress the thermal error. One plausible approach is to enhance the addition energy of the QD, thereby preventing thermally excited electrons tunneling from the leads into the QD. To the best of our knowledge, such a method has not been demonstrated to date due to insufficiently large charging energy [24, 35].

In this work, we use a silicon QD, fabricated employing a MOS planar gate stack technology [37], to demonstrate high-accuracy SE pumping in the regime where thermal errors are dominant. We use specially engineered confinement gate electrodes to enhance the electrostatic confinement of the QD [25]. A finite element analysis (FEA) of our device architecture indicates that, by tuning the electrostatic confinement, the addition energy can be as high as 17 meV. Fits of the measurement data to a thermal model yield a theoretical lower bound of 4 parts per billion (ppb) for the thermal error on the ef current plateau at $f = 1$ GHz. In addition, we experimentally measured the pump current using a high-accuracy measurement set-up, which compares the pump current to a reference current derived from primary voltage and resistance standards [17]. We found that the averaged current on the plateau, induced by a sine wave drive in the absence of magnetic field, matches the ef value well within the measurement uncertainty of ~ 0.3 ppm.

II. DEVICE ARCHITECTURE AND EXPERIMENTAL METHODS

The sample used in the experiments was fabricated on a high-purity near-intrinsic silicon wafer. We thermally grow 7 nm high quality SiO_2 gate oxide on top of the substrate. Three layers of aluminium gate electrodes are lithographically defined on top of the gate oxide. Between each layer, the sample is heated up to 150 °C in air to form an aluminium oxide coating on the electrode surface. This coating provides good electrical insulation between different metal layers [38].

A scanning electron microscope image of the aluminum gate stack of a device similar to the one used in the experiments is shown in Fig. 1(a). These metal gates, connected to programmable dc voltage sources through 200 Hz low-pass filters, can locally induce two dimensional electron gas (2DEG) channels or potential barriers at the Si/SiO_2 interface. By tuning the individual gate voltages, a quantum dot containing a few conduction electrons can be defined below the plunger gate (PL) as shown in Fig. 1(a). Electron reservoirs are accumulated below the source lead (SL) and the drain lead (DL), electrically connecting the quantum dot to the ohmic contacts.

We optimized the pump performance using a normal-accuracy measurement set-up shown in Fig. 1(a). The pump current, I_P, is measured by a low-noise transimpedance amplifier (Femto DDPCA300) connected to the drain contact. The reference current source used in high-accuracy measurement is also connected to the drain and is switched off ($V = 0$) in the normal-accuracy measurement set-up. We operate the SE pump with a sinusoidal excitation. As shown in Fig. 1(b), each pumping cycle begins with the rf drive lowering the potential barrier between the QD and the source reservoir and loading the QD with electrons. Then the rf drive raises the barrier to trap electrons and eject some or all of them to the drain reservoir. Gate B1 was driven by a microwave source (HP8341B) through a room temperature bias-tee followed by a 9 dB attenuator. The source was synchronized to a 10 MHz reference frequency derived from a primary caesium frequency standard. All RF power levels quoted in this paper refer to the power after the 9 dB attenuator. All measurements presented in this work were

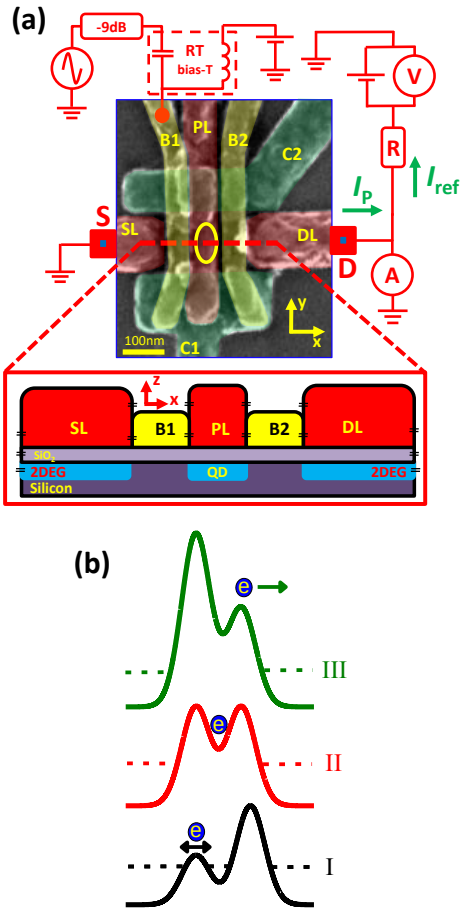

FIG. 1. (a) False-color scanning electron microscope image of an electron pump similar to the one used. The yellow circle highlights the approximate region where a quantum dot is formed. A schematic of the measurement set-up as well as an illustrative cross-sectional view of the metal-oxide-semiconductor structure are also shown. The drain contact is connected to the reference current source used in the high-accuracy measurements. It consists of a temperature controlled 1 GΩ thick-film resistor and a voltage source (Keithley213) monitored by a high-accuracy voltmeter (HP 3458A). (b) Sketch of the conduction band energy profile (solid lines) and fermi-level (dashed lines) during a pumping cycle.

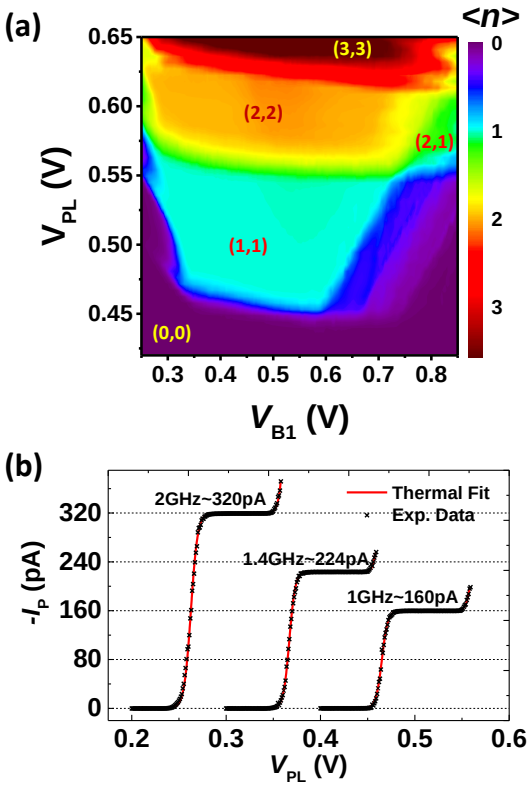

FIG. 2. (a) Coarsely tuned current plateaux at $f = 500$ MHz measured by the normal-accuracy set-up. In the notation (m,n), m (n) represents the ideal number of captured (ejected) electrons. Here, $V_{SL} = V_{B2} = 1.5$ V, $V_{DL} = 1.75$ V, $V_{C1} = -1$ V, $V_{C2} = 0.2$ V and $P_{B1} = 2$ dBm. (b) Normal-accuracy measurements (black crosses) of pumped current as a function of plunger gate voltage for different pumping frequencies and fits to the thermal model (red solid lines). Data have been horizontally shifted for clarity. Parameter settings: $V_{SL} = V_{B2} = 1.5$ V, $V_{B1} = 0.45$ V, $V_{DL} = 1.9$ V, $V_{C1} = -1.04$ V, $V_{C2} = 0.187$ V and $P_{B1} = 3$ dBm.

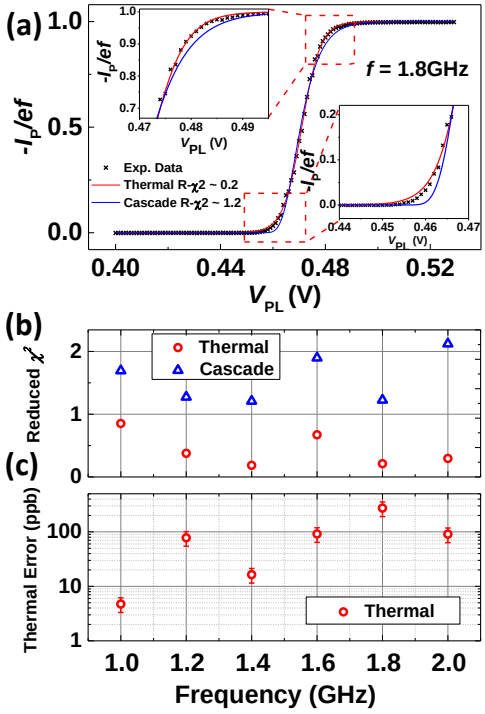

FIG. 3. (a) Normal-accuracy measurement (black crosses) of pumped current plateau as a function of plunger gate voltage and its fits to thermal (red solid line) and decay cascade model (blue solid line). Insets: selected data from the main panel on expanded axes. (b) The reduced χ^2 fit error as a function of pumping frequency for both thermal and decay cascade models. (c) The thermal error at the center of the first plateau calculated according to the fit to the thermal model at different frequencies. The center point is defined as the point of inflection on that current plateau, predicted by the thermal fit. The red error bar represents the typical error of the fit (~10%). For (a), (b) and (c), all gate voltage settings and rf power level are identical to Fig. 2(b).

carried out on a single device in the absence of a magnetic field with a small (~ 250 μV) stray bias across the pump due to the current preamplifier. The sample was cooled in a helium-3 cryostat with a base temperature of 300 mK.

We take the following approach to search for a stable low-error current plateau: First, the capacitive coupling strength of the quantum dot to each gate is obtained from the period of the corresponding Coulomb blockade oscillations. Second, the two gate voltages that have the strongest capacitive coupling to the dot potential, namely, V_{B1} and V_{PL}, are selected to be the main sweeping parameters. Third, a sinusoidal excitation with relatively low frequency, starting from 500 MHz, is applied to B1. We gradually increase the rf drive power, P_{B1}, until a plateau structure, shown in Fig. 2(a), appears in the V_{B1} – V_{PL} plane. Finally, we decrease V_{C1} and V_{C2} below the threshold voltage to obtain a flatter current plateau [25]. We verify the robustness of the well optimized current plateau at high pumping frequencies. As shown in Fig. 2(b), the ef current plateau is well pronounced up to 2 GHz without changing the gate voltages or rf power.

III. RESULTS

A. SE Pumping in the Thermal Regime

The shape of the current staircase between two adjacent plateaux as a function of the QD depth-tuning gate V_{PL} (Fig. 2(b)) provides information about the process by which the QD is decoupled from the source lead. To date, reported accurate semiconductor pumps [17, 18, 27, 32] have operated in the decay-cascade regime [34]. The final number of electrons in the QD is determined by a one-way cascade of back-tunneling events [34], characterized experimentally by an asymmetric staircase modelled using a double-exponential function. In this work, we consider the possibility that the electron reservoir is heated

by the large-amplitude sinusoidal wave drive, leading to the charge capture in thermal regime. In this regime, the average number of captured electrons, $\langle m \rangle$, can be expressed as a cascaded Fermi function of $V_{\rm PL}$:

$$\begin{aligned} \langle m \rangle &= \sum 1/\{1+\exp[E_{\rm add}^{(\rm n)}/(k_{\rm B}T)]\} \\ &= \sum 1/[1+\exp(A_{\rm n}+B_{\rm n}V_{\rm PL})], \end{aligned} \tag{1}$$

where, $E_{\rm add}^{(\rm n)}$ is the addition energy of the nth electron, and $A_{\rm n}$ and $B_{\rm n}$ are the fit parameters for the nth current plateau. As is clear from Fig. 3(a), the current staircase of our device is better described by the thermal model than the decay cascade model. The reduced χ^2 fit error for the thermal model, displayed in Fig. 3(b), is significantly lower than that for the decay cascade model for all studied pumping frequencies. This strongly suggests our device is indeed operating in the thermal regime.

We estimated the reservoir electron temperature for the measurement in Fig. 3 using the following method. We extract the ratio of $E_{\rm add}/k_{\rm B}T$ from the thermal fits presented in Fig. 3. Along with an addition energy of 17 meV, calculated based on a conduction band profile simulated in the commercial semiconductor software package ISE-TCAD[39], we deduced the local electron temperature near the SE pump to be around 9 K at a $f = 1$ GHz. We need to estimate the addition energy using a simulation because the tunnel barriers are made completely opaque in the SE pumping regime in order to prevent co-tunneling errors [40], which prevents the direct observation of the $E_{\rm add}$ in conductance measurements. More details on the TCAD simulation and the estimation of the QD addition energy are presented in the supplementary information.

In our previous work, a device with identical design driven by a much smaller rf signal, ~ -6 dBm, demonstrated SE pumping in the decay cascade regime [25]. This suggests that the thermal regime observed in the present experiments is indeed due to heating of the electron reservoirs by the large rf drive signal. A similar heating effect has been observed in a SE shuttle fabricated employing the same silicon technology [24]. An effective electron temperature of 7 K, attributed to rf-induced heating, has also been reported in another SE pumping study employing a silicon nanowire device [35].

We now turn to investigate the impact of this localized heating on the accuracy of SE pumping. Since our pump operated in the thermal regime, the main cause of error is expected to be thermal fluctuations of the QD electron number during its decoupling from the source reservoir [35]. The thermal error rate at the optimal working point of the $I = ef$ plateau can be estimated as $P_{\rm error}^{\rm thermal} = 1 - 1/\{1+\exp[E_{\rm add}^{(1)}/(k_{\rm B}T)]\}$ [35], with the optimal working point given by the point of inflection of the fit line. Figure 3(c) plots the thermal error rate as a function of frequency. Despite the elevated electron temperature, we find the thermal error is as low as 4 ppb for $f = 1$ GHz.

B. High-Accuracy Measurement

To experimentally investigate the quantised current accuracy, we employ the high-accuracy measurement scheme described in Ref. [17]. We compare the pumped current, $I_{\rm P}$, to a reference current, $I_{\rm ref}$, with traceability to primary voltage and resistance standards. The transimpedance amplifier is used to measure the difference between these currents, $I_{\rm null}$. Because it measures a very small signal, the drift in gain of the transimpedance amplifier, for example due to temperature fluctuations, introduces only a small contribution to the overall uncertainty.

In previous studies employing the same measurement set-up [17, 27, 32], the 0.8 ppm systematic uncertainty in the calibration of the 1 GΩ resistor was by far the dominant contribution to the uncertainty budget. In this work, we introduce a revised uncertainty budget following a first-principles re-evaluation of the cryogenic current comparator (CCC) bridge used to calibrate the resistor [41]. In the revised uncertainty budget, the largest systematic term is 0.1 ppm, due to the 10 MΩ reference resistor used in the calibration, and the statistical uncertainty in the resistor calibration is also of order 0.1 ppm. A recent comparison of precision reference current sources [42] has highlighted problems with short-term drift affecting high-value standard resistors. To reduce the impact of this drift on the pump measurements to well below 0.1 ppm, in this work we calibrated the 1 GΩ resistor very frequently, with an interval between calibrations as short as 2 days. More information about the precision measurement technique, including a breakdown of the uncertainty budget, is given in the supplementary information.

We carried out our high accuracy measurement on an optimized $I = ef$ plateau at 1 GHz. The pumped current as a function of $V_{\rm PL}$ is shown in Fig. 4(a), where the fractional deviation of the pump current from ef is defined as $\Delta I_{\rm P} \equiv (I_{\rm P} - e_{90}f)/e_{90}f$. We use $e_{90} \equiv 2/(R_{\text{K-90}}K_{\text{J-90}})$ to maintain consistency of units, since $I_{\rm ref}$ is derived from primary voltage and resistance standards using the conventional 1990 values $K_{\text{J-90}}$ and $R_{\text{K-90}}$ for the Josephson and von Klitzing constants respectively [43]. The normalised difference between e_{90} and the latest SI (CODATA 2014) value of e is $(e_{90} - e)/e_{90} = -8.06 \times 10^{-8}$ [44], so consistency of unit systems is an important consideration as the total measurement uncertainty approaches the 0.1 ppm level.

We define the plateau as the region where the fit of the thermal model deviates from the true ef value by less than 0.03 ppm. We show these data points on the plateau in the inset of Fig. 4(a). Averaging these points, we obtain $\Delta I_{\rm P} = 0.071$ ppm. We take the error of the mean over the data points collected at these 8 different $V_{\rm PL}$ as the relative statistical (type A) uncertainty for the measurement of the pump current, $U_{\rm A} = 0.237$ ppm. The total relative measurement uncertainty of the pump current is $U_{\rm total} = \sqrt{U_{\rm A}^2 + U_{\rm B}^2} = 0.31$ ppm. Thus the pump

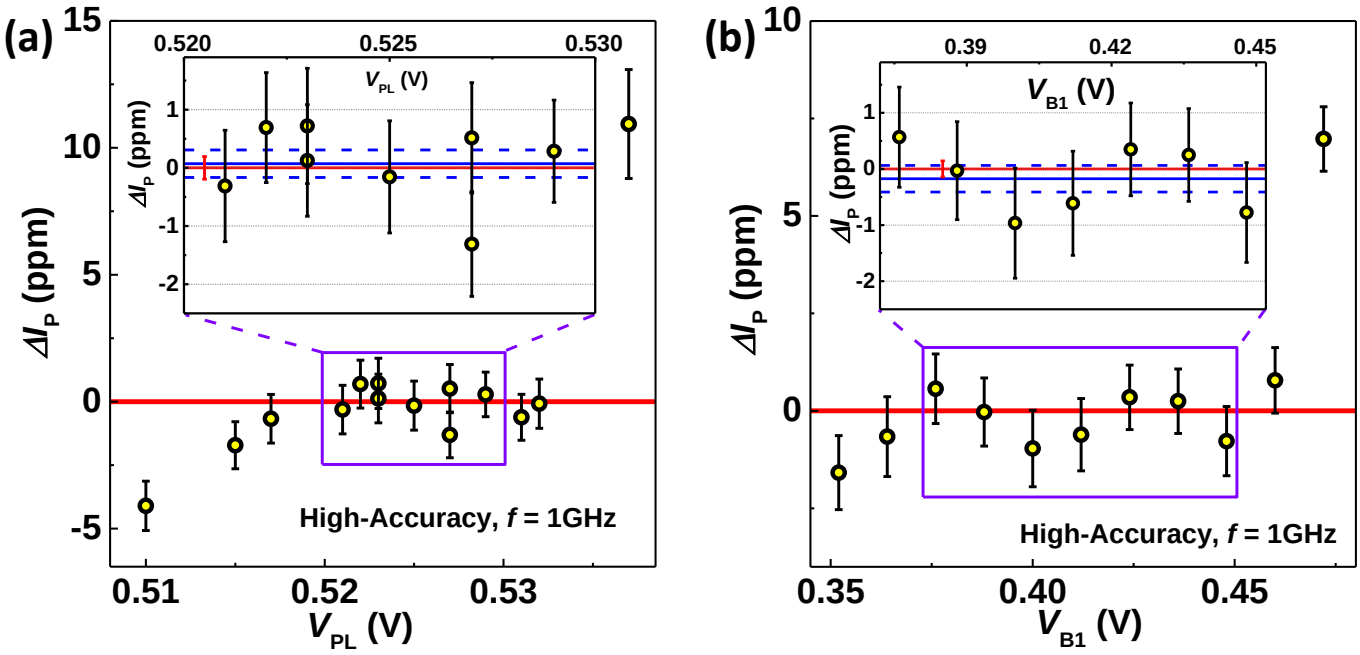

FIG. 4. High-accuracy measurements of relative deviation $\Delta I_{\rm P}$ of pump current $I_{\rm P}$ from the ideal ef value as functions of (a) $V_{\rm PL}$ and (b) $V_{\rm B1}$ at $f = 1$ GHz. Each data point is obtained by averaging 85 minutes of raw data. The black error bar represents the 1σ relative statistical uncertainty over each 85-mins measurement, which is typically ~ 0.9 ppm. The red solid line indicates $I_{\rm P} = ef$. We define the current plateau as the region where the fit of the thermal model deviates from the true ef value by less than ± 0.03 ppm. Insets: Data points in the current plateau region on expanded axes. The red error bar corresponds to the relative systematic uncertainty for the measurement of $I_{\rm ref}$. The blue solid (dashed) line corresponds to the mean (error of the mean) of the points on the plateau. All the uncertainties quoted in this paper are 1σ and have been rounded up to the next 0.01 ppm. The parameter settings are the same as in Fig. 2(b), except $V_{\rm PL} = 0.525$ V for (b).

current averaged over the plateau can be expressed as $\Delta I_{\rm P} = (0.071 \pm 0.31)$ ppm. To verify the robustness of our device, we also carried out another high accuracy scan by stepping $V_{\rm B1}$. By repeating the similar procedure, we find the pump current averaged over the plateau, shown in the inset of Fig. 4(b), to be $\Delta I_{\rm P} = (-0.174 \pm 0.27)$ ppm. The deviation of the pump current from ef is well within the measurement uncertainty, and represents the most accurate measurement to date on a silicon SE pump.

IV. SUMMARY AND OUTLOOK

Despite severe heating in the electron reservoir, the electron pump presented in this work generated a pump current equal to ef within the ~ 0.3 ppm measurement uncertainty at $f = 1$ GHz. Furthermore, fitting the data to a thermal capture model indicates a theoretical lower bound for the pumping error of 4 ppb at the center of the first current plateau. This suggests that our pump may satisfy the stringent accuracy requirements for a metrological current source [1, 6, 7]. This work clearly indicates that the large addition energy of a small silicon QD can suppress thermal errors and lead to accurate gigahertz SE pumping in the thermal regime. In addition, the fact that strong magnetic fields or tailored waveform drives are not required for the accurate operation of our pump, could greatly simplify the experimental implementation of the new standard of electrical current.

Note that one could potentially reduce the reservoir electron temperature, which will significantly improve the accuracy of our pump in the thermal regime, by adopting a three-waveform pumping scheme [26]. This technique may reduce the rf amplitude required to pump the electrons and mitigate the drive induced heating in the source reservoir.

ACKNOWLEDGMENTS

We thank T. Tanttu and K. W. Chan for enlightening discussions and valuable feedback on the manuscript. This work is supported by Australian Research Council (Grant No. DP120104710 and DP160104923), the U.S. Army Research Office (W911NF-13-1-0024), the Academy of Finland through its Centre of Excellence Programme (Grant No. 284621), the project EMPIR 15SIB08 e-SI-Amp, and the UK department for Business, Innovation, and Skills. This project has received funding from the EMPIR programme co-financed by the Participating States and from the European Unions Horizon 2020 research and innovation programme. We acknowledge the Australian National Fabrication Facility for the support in device manufacturing. A.R. ac-

knowledges support from the European Union's Horizon 2020 research and innovation programme under the Marie Sklodowska-Curie grant agreement No 654712 (SINHOPSI).

[1] J. P. Pekola, O.-P. Saira, V. F. Maisi, A. Kemppinen, M. Möttönen, Y. A. Pashkin, and D. V. Averin, Rev. Mod. Phys. **85**, 1421 (2013).

[2] B. Kaestner and V. Kashcheyevs, Rep. Prog. Phys. **78**, 103901 (2015).

[3] M. Kataoka, N. Johnson, C. Emary, P. See, J. P. Griffiths, G. A. C. Jones, I. Farrer, D. A. Ritchie, M. Pepper, and T. J. B. M. Janssen, Phys. Rev. Lett. **116**, 126803 (2016).

[4] J. D. Fletcher, P. See, H. Howe, M. Pepper, S. P. Giblin, J. P. Griffiths, G. A. C. Jones, I. Farrer, D. A. Ritchie, T. J. B. M. Janssen, and M. Kataoka, Phys. Rev. Lett. **111**, 216807 (2013).

[5] N. Ubbelohde, F. Hohls, V. Kashcheyevs, T. Wagner, L. Fricke, B. Kästner, K. Pierz, H. W. Schumacher, and R. J. Haug, Nature nanotechnology **10**, 46 (2015).

[6] F. Piquemal and G. Genevs, Metrologia **37**, 207 (2000).

[7] M. W. Keller, J. M. Martinis, N. M. Zimmerman, and A. H. Steinbach, Appl. Phys. Lett. **69**, 1804 (1996).

[8] M. W. Keller, A. L. Eichenberger, J. M. Martinis, and N. M. Zimmerman, Science **285**, 1706 (1999).

[9] J. Shilton, V. Talyanskii, M. Pepper, D. Ritchie, J. Frost, C. Ford, C. Smith, and G. Jones, J. Phys. Condens. Matter **8**, L531 (1996).

[10] V. Talyanskii, J. Shilton, M. Pepper, C. Smith, C. Ford, E. Linfield, D. Ritchie, and G. Jones, Phys. Rev. B **56**, 15180 (1997).

[11] A. O. Niskanen, J. M. Kivioja, H. Seppä, and J. P. Pekola, Phys. Rev. B **71**, 012513 (2005).

[12] J. J. Vartiainen, M. Möttönen, J. P. Pekola, and A. Kemppinen, Appl. Phys. Lett. **90**, 082102 (2007).

[13] M. Möttönen, J. J. Vartiainen, and J. P. Pekola, Physical review letters **100**, 177201 (2008).

[14] J. P. Pekola, J. J. Vartiainen, M. Möttönen, O.-P. Saira, M. Meschke, and D. V. Averin, Nat. Phys. **4**, 120 (2008).

[15] M. Blumenthal, B. Kaestner, L. Li, S. Giblin, T. Janssen, M. Pepper, D. Anderson, G. Jones, and D. Ritchie, Nat. Phys. **3**, 343 (2007).

[16] X. Jehl *et al.*, Phys. Rev. X **3**, 021012 (2013).

[17] S. Giblin, M. Kataoka, J. Fletcher, P. See, T. Janssen, J. Griffiths, G. Jones, I. Farrer, and D. Ritchie, Nat. Commun. **3**, 930 (2012).

[18] F. Stein *et al.*, Appl. Phys. Lett. **107**, 103501 (2015).

[19] S. Giblin, P. See, A. Petrie, T. Janssen, I. Farrer, J. Griffiths, G. Jones, D. Ritchie, and M. Kataoka, Appl. Phys. Lett. **108**, 023502 (2016).

[20] M. Connolly, K. Chiu, S. Giblin, M. Kataoka, J. Fletcher, C. Chua, J. Griffiths, G. Jones, V. Fal'Ko, C. G. Smith, and T. J. B. M. Janssen, Nat. Nanotech. **8**, 417 (2013).

[21] A. Fujiwara, N. M. Zimmerman, Y. Ono, and Y. Takahashi, Appl. Phys. Lett. **84**, 1323 (2004).

[22] A. Fujiwara, K. Nishiguchi, and Y. Ono, Appl. Phys. Lett. **92**, 2102 (2008).

[23] Y. Ono and Y. Takahashi, Appl. Phys. Lett. **82**, 1221 (2003).

[24] K. Chan, M. Möttönen, A. Kemppinen, N. Lai, K. Tan, W. Lim, and A. Dzurak, Appl. Phys. Lett. **98**, 212103 (2011).

[25] A. Rossi, T. Tanttu, K. Y. Tan, I. Iisakka, R. Zhao, K. W. Chan, G. C. Tettamanzi, S. Rogge, A. S. Dzurak, and M. Möttönen, Nano Lett. **14**, 3405 (2014).

[26] T. Tanttu, A. Rossi, K. Y. Tan, A. Mäkinen, K. W. Chan, A. S. Dzurak, and M. Möttönen, Scientific Reports **6**, 36381 (2016).

[27] G. Yamahata, S. P. Giblin, M. Kataoka, T. Karasawa, and A. Fujiwara, Appl. Phys. Lett. **109**, 013101 (2016).

[28] G. Yamahata, K. Nishiguchi, and A. Fujiwara, Nat. Commun. **5**, 5038 (2014).

[29] G. Tettamanzi, R. Wacquez, and S. Rogge, New J. Phys. **16**, 063036 (2014).

[30] G. Lansbergen, Y. Ono, and A. Fujiwara, Nano Lett. **12**, 763 (2012).

[31] B. Roche, R.-P. Riwar, B. Voisin, E. Dupont-Ferrier, R. Wacquez, M. Vinet, M. Sanquer, J. Splettstoesser, and X. Jehl, Nat Commun. **4**, 1581 (2013).

[32] M.-H. Bae, Y.-H. Ahn, M. Seo, Y. Chung, J. D. Fletcher, S. P. Giblin, M. Kataoka, and N. Kim, Metrologia **52**, 195 (2015).

[33] F. Stein, H. Scherer, T. Gerster, R. Behr, M. Götz, E. Pesel, C. Leicht, N. Ubbelohde, T. Weimann, K. Pierz, *et al.*, Metrologia **54**, S1 (2016).

[34] V. Kashcheyevs and B. Kaestner, Phys. Rev. Lett. **104**, 186805 (2010).

[35] G. Yamahata, K. Nishiguchi, and A. Fujiwara, Phys. Rev. B **89**, 165302 (2014).

[36] V. Kashcheyevs and J. Timoshenko, in *Precision Electromagnetic Measurements (CPEM 2014), 2014 Conference on* (IEEE, 2014) pp. 536–537.

[37] S. J. Angus, A. J. Ferguson, A. S. Dzurak, and R. G. Clark, Nano Lett. **7**, 2051 (2007).

[38] A. Rossi, T. Tanttu, F. E. Hudson, Y. Sun, M. Möttönen, and A. S. Dzurak, J. Vis. Exp. **100**, e52852 (2015).

[39] M. E. Law and S. M. Cea, Computational Materials Science **12**, 289 (1998).

[40] H. Pothier, P. Lafarge, C. Urbina, D. Esteve, and M. Devoret, EPL **17**, 249 (1992).

[41] S. Giblin, Unpublished.

[42] D. Drung, C. Krause, S. P. Giblin, S. Djordjevic, F. Piquemal, O. Séron, F. Rengnez, M. Götz, E. Pesel, and H. Scherer, Metrologia **52**, 756 (2015).

[43] N. M. Zimmerman, American Journal of Physics **66**, 324 (1998).

[44] P. J. Mohr, D. B. Newell, and B. N. Taylor, Journal of Physical and Chemical Reference Data **45**, 043102 (2016), reference on page 65.

[45] T. Thorbeck and N. M. Zimmerman, AIP Advances **5**, 087107 (2015).

[46] D. W. Allan, IEEE Transactions on instrumentation and measurement **1001**, 646 (1987).

V. SUPPLEMENTARY INFORMATION

A. Conduction Band Energy Profile Simulation

In this work, we estimate the addition energy of the QD based on the conduction band energy profile (E_{CB}) simulated using the commercial semiconductor software ISE-TCAD [39]. This package can replicate the electrostatic potential profile, in bulk semiconductors, by iteratively solving Poisson's equation attached to the user-defined mesh grid at low temperatures. The software package can also conveniently translate the electrostatic potential profile into the E_{CB} landscape. The simulated model, based on the geometry of the device used in the experiments, is presented in Fig. S1(a). The measured threshold voltage of 0.4 V corresponds to a Si/SiO_2 interface charge density of $Q_{\mathrm{ox}} = -1.45 \times 10^{11}$ cm^{-2} in the TCAD simulation. The metal-gate-induced strain, not considered by the ISE-TCAD package, could potentially affect the QD formation in our device architecture [45]. For the purpose of matching the simulation to the experiment, we choose to compensate the effect of the strain through adjustment in gate voltages. Note that our previous work clearly demonstrates that the enhancement of the addition energy imposed by the gate C1 and C2 is electrostatic [25]. Hence, we assume that the enhancement in electrostatic confinement is not affected by strain effects, and can be accurately captured in a pure-electrostatic simulation using the TCAD. We calibrate the gate voltages as follows: First, we simulate the E_{CB} profile of a QD similar to the one measured in a dc source-drain bias scan in Fig. S1(b). The measurement is carried out in the weak electrostatic confinement regime, where the source-drain conductance is still measurable. We use all gate voltages from the experiment and keep the source-drain bias voltage, V_{DS}, at zero. We adjust the voltages V_{B1} and V_{B2} in the simulation until the estimated addition energy of the QD matches with the experimental result (≈ 3 meV). Using these calibrated barrier gate voltages ($V_{\mathrm{B1}} = V_{\mathrm{B2}} = 0.34$ V), we simulated the E_{CB} profile of the QD under the condition that closely resembles the SE pumping experiment in Fig. 3. The sliced E_{CB} profiles through the center of the QD are presented in Fig. S1(c) and (d).

B. Estimation of the Addition Energy

From the gradient of the edge of the coulomb blockade region, marked with the red solid line in Fig. S1(b), we acquire the ratio $m_+ = C_{\mathrm{g}}/(C_\Sigma - C_{\mathrm{s}})$, where C_{g} is the capacitance between the QD and gate PL, C_Σ is the total capacitance between the QD and surrounding environment and C_{s} is the capacitance between the QD and source reservoir. Similarly, we can derive the ratio $m_- = C_{\mathrm{g}}/C_{\mathrm{s}}$ from the edge marked with the blue solid line in Fig. S1(b). Combining these two expressions gives the ratio between the capacitances C_Σ and C_{g}. In our previous study [25], we have experimentally demonstrated, using a device with identical design, that the edge gradient of the coulomb blockade region is insensitive to the changes in the confinement gate voltages V_{C1} and V_{C2}. This implies that the ratio C_Σ/C_{g} does not change significantly when electrostatic confinement increases. We also confirm, in the measurement of another identical SE pump, that the ratio C_Σ/C_{g} does not change with V_{PL} even in the few-electron regime. We estimate the gate capacitance C_{g} using the parallel plate capacitance model, $C_g = \epsilon \times A/d$, where ϵ is the dielectric constant of SiO_2, d is the thickness of the gate oxide and A is the area of the QD in the plane of the Si/SiO_2 interface. We acquire the parameter A from the sliced 2D profile of the simulated E_{CB} 0.1 nm below the interface.

C. High-Accuracy Measurement

1. *On-Off Cycle Averaging Technique*

Figure S2(b) shows the Allan deviation of the pump current as a function of averaging time obtained from a time series of continuously acquired data with the pump and reference currents both turned on. There is a clear transition from white (frequency-independent) noise, yielding a $1/\sqrt{t}$ behavior, to $1/f$ noise, yielding a flat behavior, for averaging times longer than ~ 40 seconds. This means that further averaging of the continuously measured pump current for times longer than this will not yield any further reduction of the statistical uncertainty[46]. The $1/f$ noise spectrum for long averaging times is caused by drift in offset currents and voltages present in the measurement circuit, for example the input offset bias current of the current preamplifier. As is standard practice in all types of precision electrical measurement, we reject experimental offsets by switching the current between two levels (in our case, on and off) with a cycle time within the white noise regime, and measuring the difference signal. Each ON or OFF

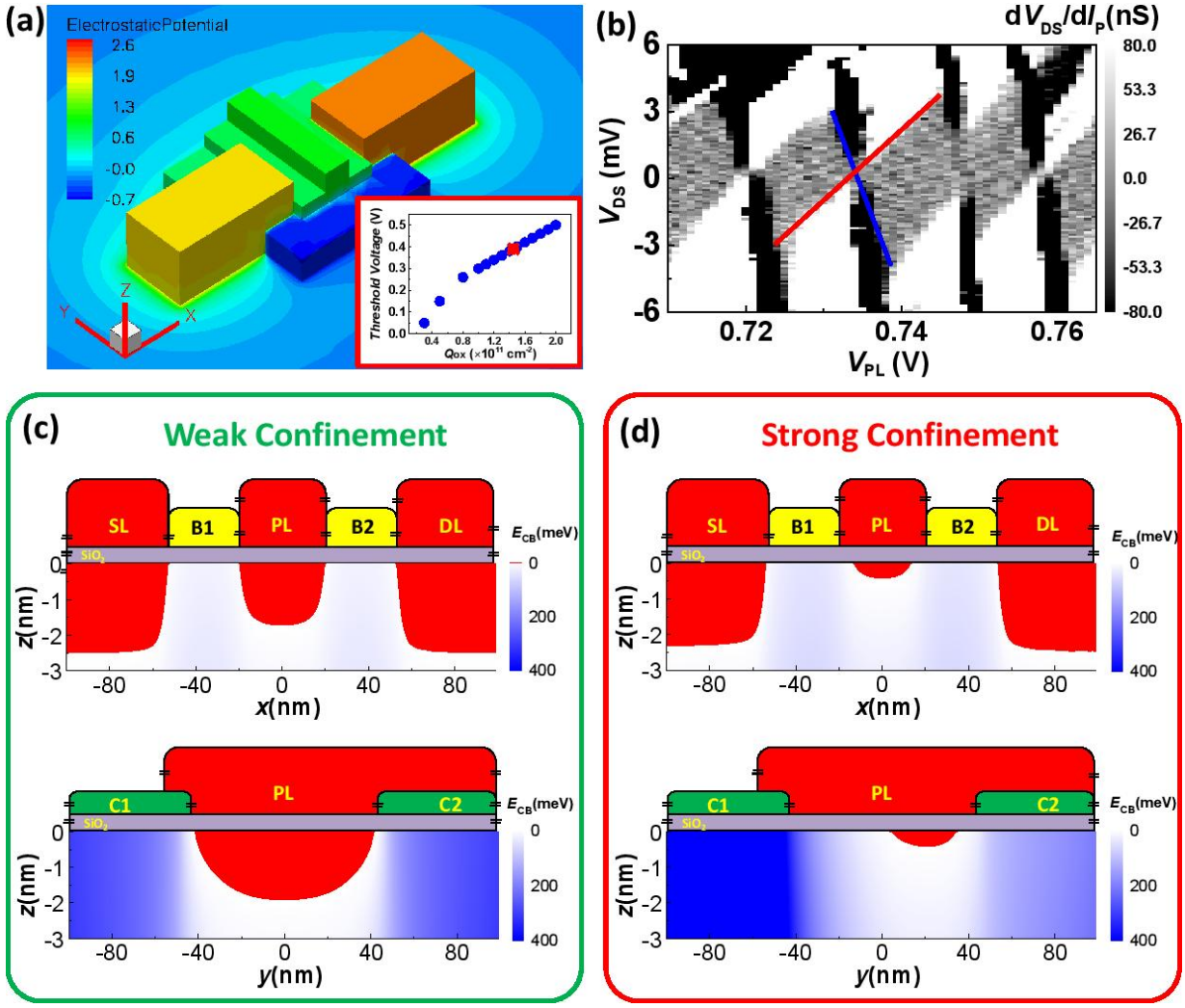

FIG. S1. (a) TCAD simulation model. Inset: The simulated threshold voltage of the device plotted as function of interface charge density $Q_{\rm ox}$. The measured threshold voltage of 0.4 V is achieved when $Q_{\rm ox} = -1.45 \times 10^{11}$ cm^{-2} (marked as red dot). (b) dc charge stability diagram of the device under weak electrostatic confinement. The grey diamond area is the coulomb blockaded region. $V_{\rm SL} = V_{\rm DL} = 1.5$ V, $V_{\rm B1} = 0.8$ V, $V_{\rm B2} = 1.4$ V, $V_{\rm C1} = 0$ V, $V_{\rm C2} = 0$ V. (c) Simulated conduction band energy ($E_{\rm CB}$) profile under weak electrostatic confinement. We used the voltage settings from (b) for this simulation except the barrier gate voltage $V_{\rm B1}$ and $V_{\rm B2}$. They are adjusted to compensate the effect of metal gate induced strain at the interface. The red region in bulk silicon represents the space where $E_{\rm CB}$ is below fermi-level. The addition energy estimated based on the simulation is 3 meV, matching up with the value we measured in (b). Gate voltage settings for (c): $V_{\rm SL} = V_{\rm DL} = 1.5$ V, $V_{\rm B1} = 0.34$ V, $V_{\rm PL} = 0.73$ V, $V_{\rm B2} = 0.34$ V, $V_{\rm C1} = 0$ V, $V_{\rm C2} = 0$ V, $V_{\rm SD} = 0$. (d) Simulated $E_{\rm CB}$ profile under strong electrostatic confinement (SE pumping regime). All gate voltages of the high-accuracy SE pumping experiment, presented in Fig. 4(a), are used in this simulation except for gate B1 and B2 where the calibrated value of $V_{\rm B1}$ and $V_{\rm B2}$ are adopted instead. The addition energy of the QD is estimated as 17 meV. Gate voltage settings for (d): $V_{\rm SL} = 1.5$ V, $V_{\rm DL} = 1.9$ V, $V_{\rm B1} = V_{\rm B2} = 0.34$ V, $V_{\rm PL} = 0.525$ V, $V_{\rm C1} = -1.04$ V, $V_{\rm C2} = 0.187$ V, $V_{\rm SD} = 0$ V. We do not consider the rf power applied to B1 in these simulations.

segment consists of 50 data points, each acquired with an integration time of 0.4 s. Raw data from several ON-OFF measurement cycles are presented in S2(c) and S2(d). After deleting 15 data points following each current switch to reject transient effects, the remaining data points from each OFF segment, and the two adjacent ON half-segments are averaged to yield $\langle I_{\rm OFF}\rangle$ and $\langle I_{\rm ON}\rangle$ respectively. The on-off difference signal $\delta I_{\rm null} = \langle I_{\rm ON}\rangle - \langle I_{\rm OFF}\rangle$, and the equivalent reference current difference $\delta I_{\rm ref}$ are used to calculate the unknown pump current.

2. Uncertainty Budget of I_P Measurement

The detailed breakdown of the uncertainty budget for the measurement of I_{P} is shown in Table I. Following standard metrological practice, uncertainty terms are distinguished as either type A (statistically evaluated) or type B (evaluated by other means). The informal categorization of uncertainties as 'random' or 'systematic' correspond in most cases to type A and type B respectively. Any uncertainties less than 0.01 ppm, for example the uncertainty in the reference frequency input to the RF source, were neglected. In the following, each component of the uncertainty budget is discussed in more detail.

1. Voltmeter type A. The Voltmeter scale factor is calibrated before and after each measurement run directly against a Josephson voltage standard. The voltmeter is calibrated *in situ*, and a low-thermal switch is used to connect its input terminals either across the voltage source, as shown in Fig. S2(a), or across the output of the Josephson array. A typical voltmeter calibration lasts around 20 minutes at a calibration voltage of 0.5 V. The type A uncertainty is evaluated as the standard error of the mean of the individual on-off cycles forming the calibration.

2. Voltmeter linearity. Because the voltmeter is calibrated at a higher voltage (0.5 V) than it is measuring during the experiment (0.16 V), some additional calibrations were performed over a range of voltages to estimate the non-linearity. The linearity correction is zero, with an uncertainty conservatively estimated as 0.03 ppm. This uncertainty term could be eliminated by performing the calibration at the same voltage as is measured during the experiment. However, this would be at the expense of a larger statistical contribution to the calibration uncertainty.

3. Voltmeter drift. The voltmeter was calibrated before and after each measurement run, yielding scale factors S_{V1} and S_{V2} respectively. The raw data was analysed using the arithmetic mean of these two scale factors to correct the voltmeter readings, and a type B uncertainty U_{drift} was calculated assuming that S_{V1} and S_{V2} define the boundaries of a square distribution: $U_{\mathrm{drift}} = |S_{\mathrm{V1}} - S_{\mathrm{V2}}|/(2\sqrt{3})$.

4. 1 GΩ type B. The resistor is calibrated in a 100 : 1 ratio measurement against a 10 MΩ resistor using a cryogenic current comparator (CCC). The 10 MΩ resistor is in turn calibrated against the quantum Hall resistance in 5 further CCC measurement steps. The 0.1 ppm type B uncertainty is the uncertainty in the value of the 10 MΩ resistor in terms of the quantum Hall resistance. Uncertainty in the 100 : 1 CCC current ratio contributes less than 0.01 ppm and is not considered.

5. 1 GΩ drift between cals. This term was evaluated in the same way as term 3.

6. 1 GΩ, type A. Typical resistor calibrations lasted around $12 - 15$ hours, with the calibration composed of hundreds of cycles each lasting ~ 100 seconds. The standard error of the mean of the individual calibration cycles if of order 0.01 ppm. However, as noted in the main text, the short-term stability of thick-film standard resistors is currently a subject of investigation and we do not assume *a priori* that these long calibrations are sampling a stationary mean. We calculate the Allan deviation of the individual calibration cycles, and conservatively evaluate the type A uncertainty as the Allan deviation for averaging times of ~ 2 hours, the longest length of time for which the Allan deviation can be reliably calculated from the calibration dataset.

7. I_{null}, type B. The 0.01% calibration uncertainty of the preamp contributes to the overall uncertainty because the preamp measures a finite current difference, ~ 3 fA, or ~ 20 ppm of the 160 pA pumped current. The product of the uncertainty and the fractional signal is $10^{-4} \times (2 \times 10^{-5}) = 2 \times 10^{-9}$, and we conservatively assign an uncertainty of 0.01 ppm.

8. I_{P}, type A. As noted in the main text, the statistical uncertainty in the pumped current, averaged over a plateau, is evaluated as the standard error of the mean of the individual data points making up the plateau. This is the largest contribution to the overall uncertainty, and is due primarily to thermal noise in the 1 GΩ reference resistor.

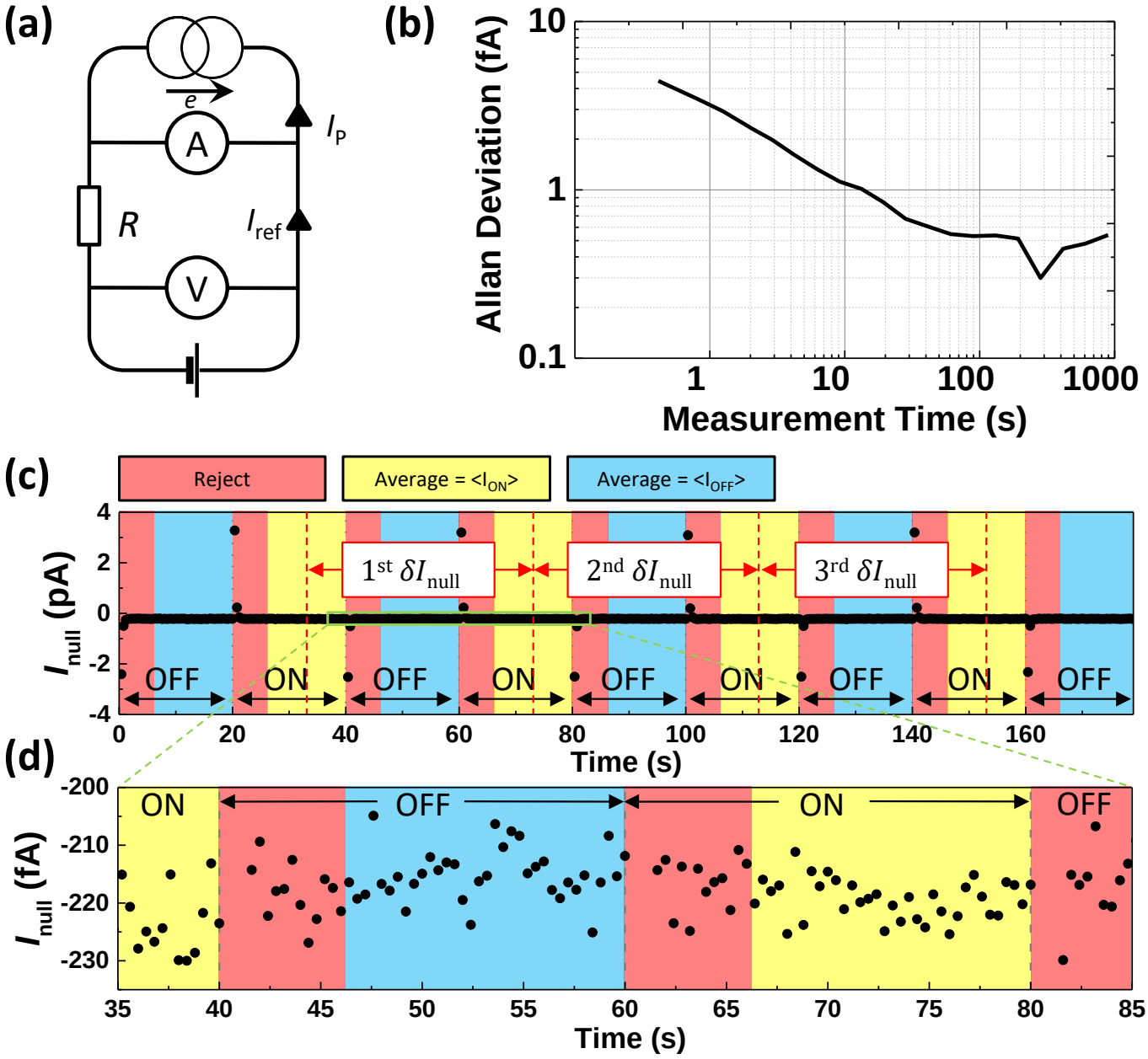

FIG. S2. (a) Circuit diagram for the high-accuracy measurement. The current, I_P, generated by the SE pump represented as the current source is balanced with a reference current I_{ref}, and hence only a small difference current, I_{null} is measured by the ammeter. The calibrations of the 1-GΩ resistor and the voltmeter provide tracebility to primary standards. (b) Allan deviation as a function of the measurement time obtained from a 20 minute time-series of I_{null} data. (c,d): raw data for on-off cycles of I_{null}. Colored boxes indicate the ranges of data rejected or averaged to calculate the ON-OFF difference $\delta I_{null} = \langle I_{ON} \rangle - \langle I_{OFF}. \rangle$

TABLE I. Breakdown of the uncertainty budget for the measurement of pumped current I_{P} from the two plateau scans reported in the main text. All reported uncertainties are dimensionless 1σ relative uncertainties in parts in 10^6.

	PL plateau (ppm)	B1 plateau (ppm)
1. Voltmeter calibration (type A)	0.01	0.01
2. Voltmeter linearity (type B)	0.03	0.03
3. Voltmeter drift (type B)	0.068	0.068
4. 1 GΩ calibration (type B)	0.1	0.1
5. 1 GΩ drift (type B)	0.01	0.01
6. 1 GΩ calibration (Type A)	0.15	0.07
7. I_{null} (type B)	0.01	0.01
8. I_{P} (type A)	0.237	0.229
Total	0.31	0.27